# Nanoelectronics and Its New Materials – A NEW ERA OF NANOSCIENCE

**Nanoelectronics and Its New Materials –**
## A NEW ERA OF NANOSCIENCE

ZEISS
Seeing beyond

WILEY

**Discover the recent advances in electronics research and fundamental nanoscience.**

Nanotechnology has become the driving force behind breakthroughs in engineering, materials science, physics, chemistry, and biological sciences. In this compendium, we delve into a wide range of novel applications that highlight recent advances in electronics research and fundamental nanoscience. From surface analysis and defect detection to tailored optical functionality and transparent nanowire electrodes, this eBook covers key topics that will revolutionize the future of electronics.

To get your hands on this valuable resource and unleash the power of nanotechnology, simply download the eBook now. Stay ahead of the curve and embrace the future of electronics with nanoscience as your guide.

ZEISS
Seeing beyond

WILEY

# Wafer-Scale Two-Dimensional Semiconductors for Deep UV Sensing

*Mustaqeem Shiffa, Benjamin T. Dewes, Jonathan Bradford,\* Nathan D. Cottam,
Tin S. Cheng, Christopher J. Mellor, Oleg Makarovskiy, Kazi Rahman, James N. O'Shea,
Peter H. Beton, Sergei V. Novikov, Teresa Ben, David Gonzalez, Jiahao Xie, Lijun Zhang,
and Amalia Patanè\**

**2D semiconductors (2SEM) can transform many sectors, from information and communication technology to healthcare. To date, top-down approaches to their fabrication, such as exfoliation of bulk crystals by "scotch-tape," are widely used, but have limited prospects for precise engineering of functionalities and scalability. Here, a bottom-up technique based on epitaxy is used to demonstrate high-quality, wafer-scale 2SEM based on the wide band gap gallium selenide (GaSe) compound. GaSe layers of well-defined thickness are developed using a bespoke facility for the epitaxial growth and in situ studies of 2SEM. The dominant centrosymmetry and stacking of the individual van der Waals layers are verified by theory and experiment; their optical anisotropy and resonant absorption in the UV spectrum are exploited for photon sensing in the technological UV-C spectral range, offering a scalable route to deep-UV optoelectronics.**

## 1. Introduction

The versatile electronic properties of 2D semiconductors (2SEM) based on van der Waals (vdW) crystals[1–7] and their compatibility with a wide range of lattice mismatched heterostructures[8–10] have generated a surge of research interest worldwide, leading to advances in science and prospects for innovative technologies.[5,11,12] Within this wide class of materials, metal chalcogenide (MC) III–VI compounds are of great interest due to their unique properties, spanning from high mobility carriers and tunable band structures to nonlinear optical responses and ferroelectricity.[13–21] In particular, for single-layer and few-layer MCs, the valence band (VB) is shaped like an inverted Mexican hat with van Hove singularities (vHs) in the density of states (DoS) and hole effective masses much heavier than in traditional semiconductors.[22–27] The interest in this unusually shaped band is motivated by the possibility to create in a semiconductor new forms of magnetic order, charge density waves, and superconductivity driven by weakly screened electron correlations.[28–30] However, the experimental observation of these phenomena, as well as the exploitation of these 2SEM, remain outstanding challenges due to a number of factors. The fabrication of high-quality MCs has proven to be difficult due to the formation of stacking faults, domain boundaries, and other crystal defects.[22] Also, the selective growth of specific stoichiometries, polymorphs, and stacking configurations of high-quality 2SEM requires advanced methods of material growth and characterization. On the other hand, crystal polymorphism offers prospects for precise engineering of electronic properties and functionalities beyond traditional systems.[31] Thus, significant efforts are directed to the use of epitaxial growth techniques,[32] such as molecular beam epitaxy (MBE),[18,22,24,25,33–37] to develop next-generation semiconductors for science and technology.

In crystallography, polymorphs are considered to be unique crystal structures of the same chemical entity; they share the same chemical compositions and bonds, but differ in their atomic arrangements. In the case of the MC GaSe, there exist several polytypes (stacking configurations) of the well-known $D_{3h}$ polymorph, shown in **Figure 1**a. The most common polytype of GaSe is referred to as $\epsilon$-GaSe.[31] The $\epsilon$-GaSe unit cell consists of two tetralayers (TLs), each constructed from a Se–Ga–Ga–Se atomic arrangement in which each Ga atom is covalently bonded to three equidistant Se atoms and another Ga

M. Shiffa, B. T. Dewes, J. Bradford, N. D. Cottam, T. S. Cheng, C. J. Mellor,
O. Makarovskiy, K. Rahman, J. N. O'Shea, P. H. Beton, S. V. Novikov,
A. Patanè
School of Physics and Astronomy
University of Nottingham
Nottingham NG7 2RD, UK
E-mail: jonathan.bradford@nottingham.ac.uk;
amalia.patane@nottingham.ac.uk

T. Ben, D. Gonzalez
University Research Institute on Electron Microscopy and Materials
IMEYMAT
Universidad de Cádiz
Cádiz 11510, Spain

J. Xie, L. Zhang
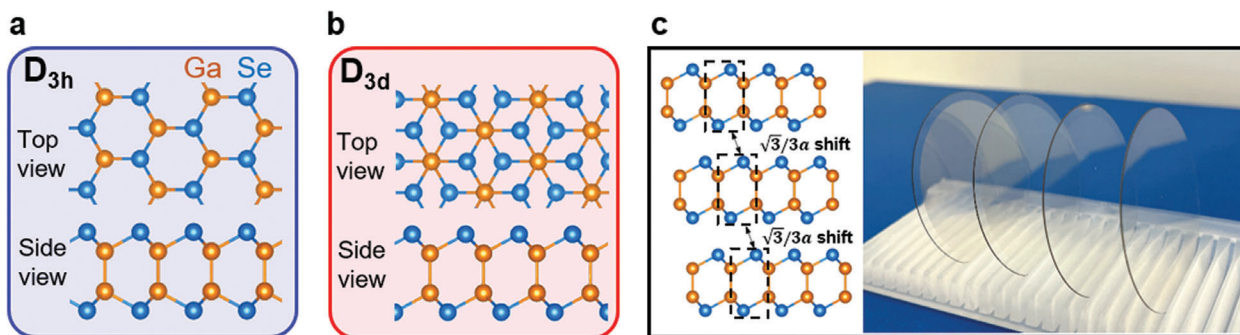College of Materials Science and Engineering
Jilin University
Changchun 130012, China

**ADVANCED
SCIENCE NEWS**

www.advancedsciencenews.com

**NANO · MICRO
small**

www.small-journal.com

**Figure 1.** In-plane and side view schematics of two polymorphs of GaSe with a) axial symmetry ($D_{3h}$) and b) centrosymmetry ($D_{3d}$). c) Left: side-view schematic of $\gamma'$-GaSe based on the ABC stacking of the $D_{3d}$ polymorph. Right: image of $\gamma'$-GaSe films with increasing thicknesses from 1 to 55 nm (right to left) grown by MBE on 2-in. diameter sapphire wafers.

atom. Most other stable forms of GaSe share the same TL structure and $D_{3h}$ symmetry, differing only in their stacking (AB or ABC) configurations. Recently, however, an additional polymorph with $D_{3d}$ symmetry has been discovered in which the Ga−Se bonds in the upper and lower layers have a rotational mismatch of 60°, as shown in Figure 1b.[38,39] The $D_{3d}$ polymorph shares its ABC-stacking configuration with the $\gamma$-GaSe polytype, in which the three constituent TLs are translationally offset by 1/3 of the unit cell in the [10$\bar{1}$0] direction. The $D_{3d}$-based polytype, referred to as $\gamma'$-GaSe, has distinct properties (e.g., harmonic generation and optical selection rules) from those of the $\gamma$-GaSe and $\epsilon$-GaSe polytypes[18,22,40,41] due to the centrosymmetry of the TL.[42] Although the experimental observation of the $D_{3d}$ polymorph of GaSe and its ABC-stacking have been reported previously, these have appeared in co-stable states with the $D_{3h}$ polymorph due to the small energy differences between their formation mechanisms.[38,39] In general, the precise engineering of physical properties and their scalability remain significant challenges, slowing down scientific advances and the adoption of new 2SEM in modern applications beyond prototype concepts.

Here, we report on the wafer-scale growth of GaSe on sapphire with a dominant $D_{3d}$ polymorph, Figure 1c. GaSe layers of well-defined thicknesses from 55 nm down to 1 nm are grown using a bespoke facility for the epitaxial growth and in situ studies of 2SEM (EPI2SEM). We present a range of in situ and ex situ studies, and theoretical modeling, including cross-sectional scanning transmission electron microscopy (STEM), Raman spectroscopy, and spectroscopic ellipsometry to verify the dominant $D_{3d}$ polymorph by comparison to density functional theory (DFT). The $D_{3d}$ polymorph is thermodynamically and kinetically stable. We exploit the ultraviolet (UV) absorption of the grown GaSe layers and their optical anisotropy, combined with the transparency of the sapphire substrate, to demonstrate deep-UV sensing. The high responsivity of the GaSe sensors in the UV range offers opportunities for UV technologies, including sensors for optical communications in the UV-C band (200–280 nm).
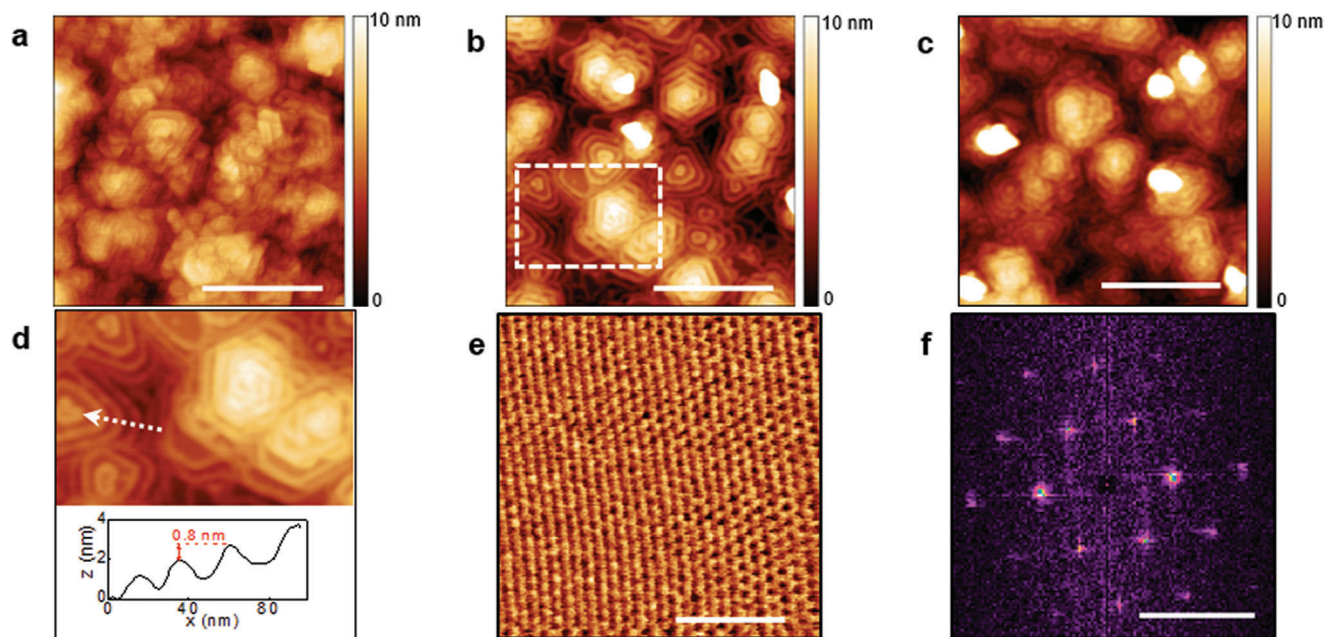
## 2. Results and Discussion

### 2.1. Scalable Growth of $\gamma'$-GaSe on Sapphire

The EPI2SEM system (Scienta Omicron) consists of an MBE growth chamber, a scanning probe microscopy (SPM) chamber,

and a chamber for electron spectroscopy for chemical analysis (ESCA). These are connected by an ultra-high vacuum (UHV) line, enabling the transfer of samples on $10 \times 10$ mm$^2$ substrates between all three chambers in vacuum. The samples can also be transported between EPI2SEM and external chambers using a vacuum suitcase at a pressure of less than $1 \times 10^{-10}$ mbar. GaSe films were grown by MBE on 2-in. diameter (Figure 1c) and $10 \times 10$ mm$^2$ $c$-plane (0001) sapphire substrates. The Ga and Se flux ratios during epitaxy were precisely controlled by the Ga effusion cell temperature and the aperture of the Se cracker valve, respectively (see Experimental Section). The growth of the layers with a range of thicknesses, $t$, from about 1 nm (single layer GaSe) to 55 nm was monitored by in situ reflection high energy electron diffraction (RHEED). After growth, samples grown on the $10 \times 10$ mm$^2$ $c$-plane (0001) sapphire were transferred via the UHV transfer line from the MBE chamber to the SPM chamber, where the surface morphology was studied by non-contact atomic force microscopy (ncAFM) (**Figure 2**a). The surface comprises islands with lateral sizes in the range of 100–200 nm. Their in-plane orientations are random with respect to the substrate surface, suggesting a lack of preferential in-plane alignment due to the weak binding of the GaSe layers to the sapphire substrate. X-ray photoelectron spectroscopy (XPS) studies confirm the stoichiometry expected for GaSe (Figure S1, Supporting Information).

GaSe layers were also imaged by AFM in ambient conditions, both immediately after removal from the UHV system (Figure 2b) and after 2 weeks of storage in a nitrogen environment and exposure to air (Figure 2c). The surface topography is mostly unchanged, save for the formation of ridges at the step edges, suggesting that oxidation occurs primarily at discontinuities in the GaSe surface. It can be seen that the terrace structure is clearly preserved even after exposure to the atmosphere. Additionally, line-profiles along the islands in the AFM image of Figure 2b,d reveal step heights of ≈0.8 nm, corresponding to the interlayer periodicity of GaSe.[43] We note that high resolution contact AFM (cAFM) images taken after 2 weeks of exposure to ambient conditions (Figure 2e,f) still distinctly reveal the lattice structure of the GaSe surface, further implying the lack of an oxide in the continuous GaSe layers. From the analysis of the cAFM images, we derive the in-plane lattice constant $a = (3.9 \pm 0.1)$ Å. This is comparable to the values predicted for the $D_{3h}$ ($a = 3.81$ Å) and $D_{3d}$ ($a = 3.82$ Å) polymorphs of GaSe.[42] AFM images of thin layers ($t$ less than or equal to 5 nm) showed surfaces with poorer

ADVANCED
SCIENCE NEWS
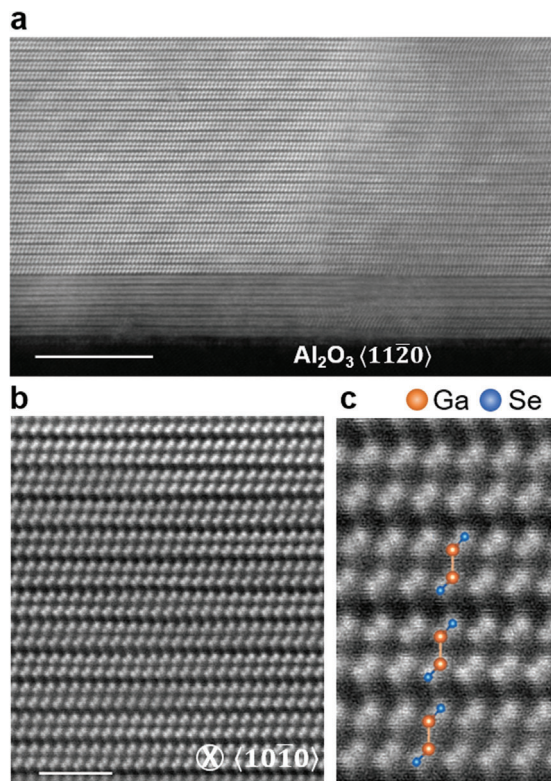www.advancedsciencenews.com

NANO · MICRO
small
www.small-journal.com

**Figure 2.** a) ncAFM image of a 55 nm-thick GaSe layer in UHV ($\Delta f$ = 70 Hz; scale bar = 300 nm). b) Tapping mode AFM image of a 24 nm-thick GaSe layer in air (scale bar = 300 nm). The white dashed square indicates the location of the AFM image shown in part (d). c) Tapping mode AFM of a 24 nm-thick GaSe layer after 2 weeks of exposure to a nitrogen environment (scale bar = 300 nm). d) AFM image and line profile along the white dashed line. e) High resolution contact-mode AFM of the sample in part (c) (scale bar = 3 nm). f) Fast-Fourier transform (FFT) of the AFM image in part (e) (scale bar = 5 nm$^{-1}$).

crystalline quality (Figure S2, Supporting Information) due to a stronger influence of the lattice mismatch between the GaSe and the sapphire substrate on the growth.

Cross-sectional aberration-corrected STEM studies and high resolution electron energy loss spectroscopy (EELS) were conducted to examine further the crystal structure and chemical composition of the grown layers (**Figure 3**a–c, for $t$ = 55 nm). The GaSe TLs near the GaSe/sapphire interface were found to be randomly oriented relative to the crystal direction. In particular, a non-homogeneous, thin ($\leqslant$ 2 nm) GaSe layer was observed at the GaSe/sapphire interface in both thin and thick samples; this does not have a sharp compositional profile and is not always present along the interface (Figure S3, Supporting Information). The GaSe TLs possess the $\gamma'$-GaSe stacking configuration in all regions studied, as shown in Figure 3b,c, and the schematic overlay in Figure 3c. Stacking faults were seen in a few locations, where the GaSe layers were rotated relative to each other (Figure S3, Supporting Information). A small misalignment of the layers may arise from the polycrystalline nature of the film. The small layer displacement may facilitate enhanced intergrain coupling in the layer plane. From the analysis of several TEM images, we deduce that the measured thickness of the single layer ([4.70 ± 0.02] Å) is smaller than that calculated in the literature for the unstrained $D_{3h}$ ($a$ = 4.88 Å) and $D_{3d}$ ($a$ = 4.87 Å) polymorphs of GaSe[42] and that predicted in this study (Table S1 and Figure S4, Supporting Information). Thus, our data suggest that the GaSe layers may be subject to in-plane tensile strain. This observation and the dominant $\gamma'$-GaSe seen in these layers are in agreement with our first-principles studies of GaSe (Table S1, Supporting

Information) and those in the literature,[42] showing that the two polymorphs have similar formation energies, but that the stability of different polymorphs and phases can be reversed by strain.

Although $\gamma'$-GaSe has been reported before,[38,39] its vibrational properties are not documented. These can provide an effective means of testing different crystal structures and their uniformity over wafer-scale samples. **Figure 4** shows the Raman spectra for a 24 nm-thick sample. They show peaks at 132, 206, 252, and 308 cm$^{-1}$. These Raman shifts are close to the $A_{1g}^1$, $E_{2g}^1$, $E_{1g}^2$, and $A_{1g}^2$ modes observed in our Bridgman-grown bulk $\epsilon$-GaSe (Figure 4a) and bulk GaSe from the literature.[44,45] However, compared to $\epsilon$-GaSe, the $E_{2g}^1$ peak is red-shifted by ≈6 cm$^{-1}$ and the $A_{1g}^2$ peak is blue-shifted by ≈2 cm$^{-1}$. This is in agreement with DFT calculations of the vibrational modes of $\gamma'$-GaSe.[39] Compared to the Bridgman-grown $\epsilon$-GaSe, the Raman peaks are also narrower, and Raman spectra measured at various points on the 2-in. diameter samples (Figure 4b) showed similar Raman shifts, indicating that the centrosymmetric polymorph is dominant throughout the MBE-grown GaSe layers and that the growth of $\gamma'$-GaSe is uniform. These properties were found to be stable over long periods of exposure of the wafer to ambient pressure, with negligible changes in the peak locations, widths, and relative intensities of the Raman modes after 1 month of storage in a nitrogen environment (Figure S5, Supporting Information). GaSe layers of different thicknesses down to $t$ = 4 nm revealed Raman shifts as shown in Figure 4 (see Figure S5, Supporting Information). However, very thin layers ($t$ ≈ 1 nm) did not produce measurable Raman signals, which we assign to the reduced volume, increased disorder, and non-resonant excitation conditions (e.g., the

**ADVANCED
SCIENCE NEWS**

www.advancedsciencenews.com
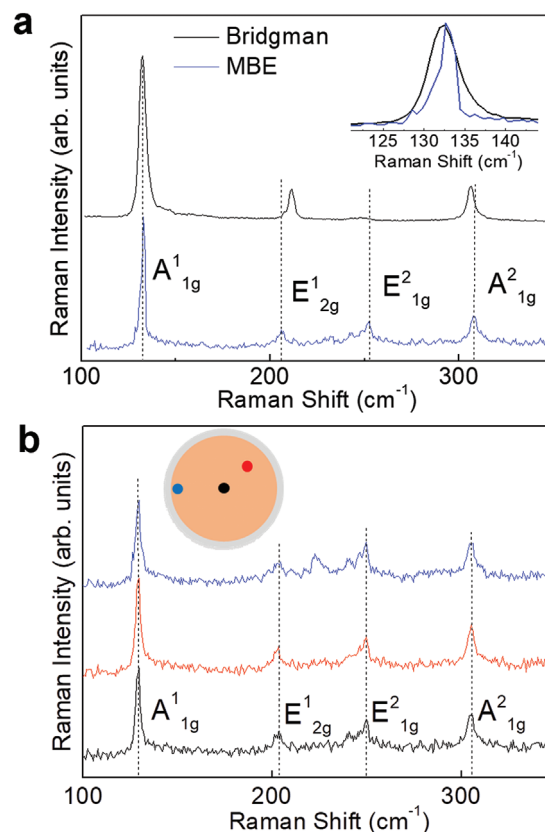
**NANO · MICRO
small**

www.small-journal.com

**Figure 3.** a) Cross-sectional high-angle annular dark-field imaging (HAADF) scanning transmission electron microscope (STEM) image of a 55 nm-thick GaSe layer on sapphire recorded along $\langle 11\bar{2}0 \rangle$ (scale bar = 10 nm). The dark region near the bottom corresponds to the sapphire substrate and the brighter region above to GaSe. b) HR-STEM image recorded along $\langle 10\bar{1}0 \rangle$ in another region of the layer (scale bar = 2 nm). c) Zoomed-in image of (b) with $\gamma'$-GaSe crystal structure overlay.



**Figure 4.** a) Raman spectra of Bridgman-grown $\epsilon$-GaSe and MBE-grown, 24 nm-thick $\gamma'$-GaSe. The inset compares the broadening for one particular Raman line. b) Raman spectra measured at various points on a 2-in. diameter for a 24 nm-thick MBE-grown GaSe sample. The inset shows the laser spot positions on the wafer for measurements displayed in the corresponding colors. All measurements were conducted in air at $T = 300$ K and laser excitation wavelength of 633 nm.

excitation laser wavelength $\lambda = 633$ nm does not match the electronic absorption bands).

## 2.2. Optical Absorption and Anisotropy

We have used variable angle spectroscopic ellipsometry (VASE) to obtain the thicknesses and optical constants (dielectric permittivity and absorption) of the grown GaSe layers in the near-infrared–visible–UV (NIR–VIS–UV) range. Ellipsometry measures the change in state of polarization of polarized light upon reflection from a surface.[46] The phase difference ($\Delta$) and amplitude ratio ($\Psi$) are related to the optical reflectance ratio, $r$, between the $p$- and $s$-polarization of light, $r_p/r_s = \tan(\Psi)e^{i\Delta}$. **Figure 5**a shows a map of the layer-thickness $t$ for a representative sample. Here, the average layer thickness is uniform across the 2-in. diameter wafer with variations in $t$ corresponding to an average surface roughness $\delta < 1$ nm. Since GaSe is a uniaxial crystal, the absorption measured by ellipsometry corresponds to the component of the absorption tensor along the direction defined by the intersection of the plane of incidence and the surface of the crystal.[47] For our experimental configuration, this corresponds to the absorption component $\alpha_{xy}$ (i.e., electric field in the layer plane $xy$). Data for the dielectric permittivity tensor are in the

Supporting Information (Figure S6, Supporting Information). As shown in Figure 5b, for all samples, the band edge absorption at $\approx 2$ eV is very weak. The absorption spectra are dominated by pronounced resonances in the UV, centered at $\approx 3.8$ eV and in the range 5–6 eV. These resonances are weakly dependent on the layer thickness, but they become broader for $t = 1$ nm. For thin layers, the ellipsometry map indicates an average layer thickness of 1.1 nm and its variation from 0.5 to 2.2 nm over a 2-in. wafer (Figure S7, Supporting Information). Our findings are in agreement with first-principles calculations by DFT showing absorption resonances in the UV range in both bulk and single layer GaSe (Figure 5c). The calculated absorption spectra reveal a strong dependence of the absorption coefficient on the polarization of light, in the directions either parallel or perpendicular to the optical $c$-axis. In particular, the band edge absorption dipole couples only weakly with light polarized in the layer plane, that is, for an electric field dipole in the layer plane. Thus, in our ellipsometry study and, more generally, under excitation of the films with light polarized in the layer plane, the absorption in the deep-UV is more strongly enhanced. The measured resonances in the deep-UV (>4.5 eV) arise from optical transitions that allow for light polarized in the layer plane, that is, optical transitions

ADVANCED
SCIENCE NEWS
www.advancedsciencenews.com

NANO · MICRO
small
www.small-journal.com
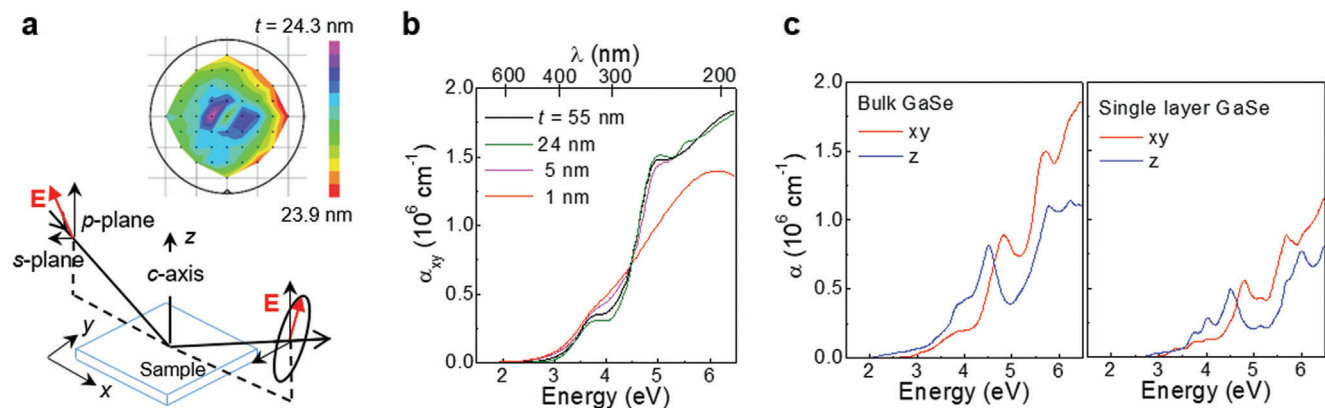
**Figure 5.** a) Schematic of ellipsometry and ellipsometry map of the layer thickness $t$ for a representative MBE-grown GaSe sample. The map is formed from measurements taken on a 5 mm square grid over the central region of a 2-in. diameter wafer using focus probes. b) Absorption spectrum of MBE-grown GaSe layers of different thickness, $t$, as measured by ellipsometry. c) Calculated absorption spectrum for bulk $\gamma'$-GaSe (left) and single layer centrosymmetric GaSe (right) for light polarized in the direction parallel ($xy$) or perpendicular ($z$) to the layer plane $xy$.

between band states with the same parity. In contrast, in the VIS range and near the band edge ($\approx 2$ eV), the measured absorption arises from states with different parity ($p$- and $s$-states in the valence and conduction bands, respectively) and is weaker.

## 2.3. UV-C Sensors

The large values of $\alpha_{xy}$ (up to $\approx 10^6$ cm$^{-1}$) in the UV-range and the transparency of the sapphire substrate to UV light offer potential for UV sensing in applications ranging from miniaturized wearable UV radiometers for healthcare to UV-C sensors for optical communication. Here, we focus on simple device architectures based on GaSe with interdigitated Au electrodes and sensing areas, $A$, of 1 mm$^2$ (**Figure 6**a). For the deposition of the Au electrodes on GaSe, a rigid metal-based shadow mask was placed in close contact with the substrate. The advantage of this approach is that it does not require coating and patterning of a photoresist on GaSe, which eliminates its exposure to polymers, solvents and/or radiation.

As shown in Figure 6a, the room temperature ($T = 300$ K) current–voltage ($I$–$V$) characteristics in the dark are symmetric with respect to the polarity of the applied voltage. The $I$–$Vs$ in the dark and under illumination with unfocused light of wavelength $\lambda = 260$ nm and power density $P = 0.7$ mW cm$^{-2}$ corresponds to an on/off ratio of $10^3$. Measurements of the photocurrent at different powers $P$ of the incident radiation give a photoresponsivity, $R$, of up to 6.4 A W$^{-1}$ ($V = 10$ V) (Figure 6b) and an external quantum efficiency EQE = $Rh\nu/e$ = 3100%.

The sensors can be switched between on and off states in a reproducible manner. We estimate the bandwidth, $Bw$, from the photocurrent rise time/decay time, $\tau$, for example, $Bw = f_{3dB}/0.886 = 250$ Hz, where $f_{3dB} = 0.35/\tau = 220$ Hz is the 3 dB bandwidth of the detector. We obtain a similar value of $Bw$ from the ac photocurrent studies (Figure 6c). Thus, we derive the specific detectivity $D^* = \sqrt{A(Bw)}/\text{NEP} \approx 4.7 \times 10^{12}$ Jones, where NEP = $I_n/R = 3.1 \times 10^{-13}$ W is the noise equivalent power and $I_n = 2.5 \times 10^{-12}$ A is the noise current, as derived from the standard deviation in the temporal fluctuations of the dark current, $I_{dark}$.
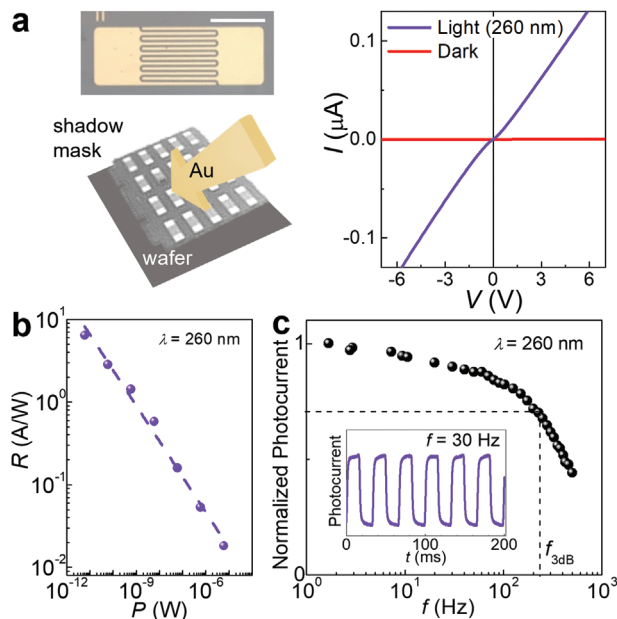


**Figure 6.** a) Left: optical image of a GaSe sensor with interdigitated contacts (scale bar = 1 mm) and schematic of shadow masking. Right: $I$–$V$ characteristics of a GaSe sensor (55 nm-thick GaSe) in the dark and under light in the UV-C band ($\lambda = 260$ nm). In the dark, the current is less than 4 nA. b) Responsivity versus incident power $P$ at $\lambda = 260$ nm. The line is a fit to the data by a power law ($R \approx P^{-0.4}$). c) Response amplitude versus frequency of light and 3 dB bandwidth ($\lambda = 260$ nm and $P = 6 \times 10^{-6}$ W). Inset: temporal response of the sensor.

As shown in **Figure 7**a, devices with different layer thickness show a strong photoresponsivity in the UV-C band. However, as the GaSe layer thickness decreases, the response becomes weaker and the peak in the dependence of $R$ on $\lambda$ shifts to shorter $\lambda$ (Figure 7b–d). For the 55 nm-thick GaSe layer, $R$ increases with decreasing $\lambda$, reaching a maximum at $\lambda = 300$ nm, followed by a monotonic decrease at shorter $\lambda$ (Figure 7b). In devices with thinner layers ($t = 24$ and 5 nm), the peak in the $R(\lambda)$ curve tends to
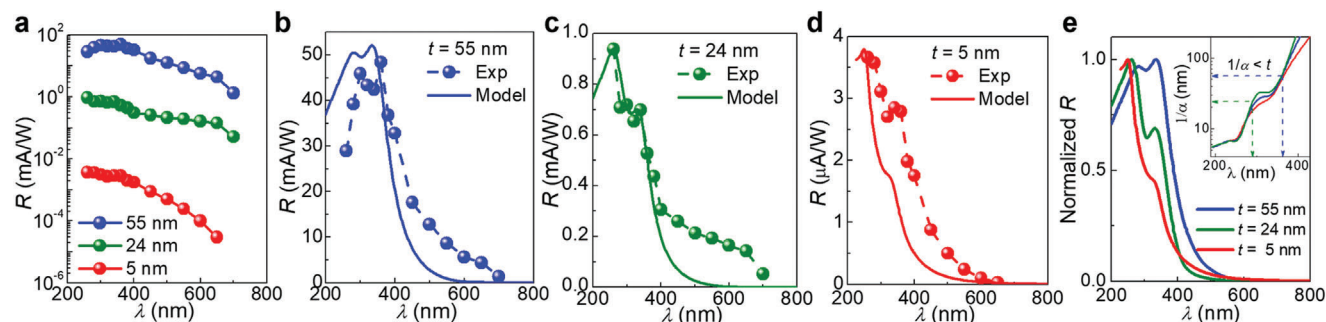
**Figure 7.** a) Responsivity, $R$, versus photon excitation wavelength $\lambda$ ($P = 0.1$ mW cm$^{-2}$) for sensors with GaSe layers of different thickness $t = 55$ nm (blue), 24 nm (green), and 5 nm (red). b–d) Calculated and measured responsivity versus $\lambda$ ($P = 0.12$ mW cm$^{-2}$) for $t = 55$ nm ($V = 10$ V) (b), $t = 24$ nm ($V = 10$ V) (c), and $t = 5$ nm ($V = 5$ V) (d). e) Calculated dependence of $R$ on $\lambda$ for different $t$. For each $t$, the $R(\lambda)$ curve is normalized to its maximum value. Inset: Dependence of the absorption length ($1/\alpha$) on $\lambda$ for samples with different $t$. The dashed arrows show the range of $\lambda$ corresponding to $1/\alpha < t$ in samples with $t = 55$ and 24 nm. For $t = 5$ nm, this condition is reached outside the measured range of $\lambda$.

shift to $\lambda = 250$ nm (Figure 7c,d). At wavelengths corresponding to large values of $\alpha$, the absorption length, $1/\alpha$, can become smaller than the layer thickness, $t$ (inset of Figure 7e). Under these conditions (e.g., $1/\alpha < t$) the layer does not contribute fully to the responsivity since the deeper sections of the layer do not absorb any photons. Thus the spectral response contrasts with the $\lambda$-dependence of the absorption, as measured by ellipsometry, but its can be explained by the dependence of the absorption depth on $\lambda$. The calculated $R(\lambda)$ curves for different $t$ (Figure 7e) are obtained using (see derivation in Section S6 and Figure S8, Supporting Information)

$$R(\lambda) = \frac{e\lambda}{hc} \frac{\tau_l}{\tau_t} [1 - \exp(-\alpha t)] \tag{1}$$

where $\tau_l$ is the lifetime of the photogenerated carriers, $\tau_t$ is the transit time of the charge carriers, $\lambda$ is the excitation wavelength, $\alpha$ is the measured absorption, and $e$, $h$, and $c$ are the electron charge, Planck's constant, and speed of light, respectively. As shown in Figure 7b–d, the spectral response of GaSe with different layer thicknesses is well described by this model. Here, we use the ratio between $\tau_l$ and $\tau_t$ as the only fitting parameter: $\tau_l/\tau_t$ is equal to $2 \times 10^{-1}$, $5 \times 10^{-3}$, and $4 \times 10^{-5}$ for $t = 55$, 24, and 5 nm, respectively. We assign the smaller value of $\tau_l/\tau_t$ in the thinner layers to a larger carrier recombination rate at the sapphire–GaSe interface and lower mobility of charge carriers. Overall, the properties of these devices compare favorably with UV-sensors from the literature, such as those reported recently for the wide band gap Ga$_2$O$_3$,[48–50] whose frequency band and on/off current ratio are both smaller than in our devices. The large optical absorption of GaSe in the UV-C band (200–280 nm range) and sensitivity to polarization of light provide a platform for advances in this important technological spectral range. The UV-C band is free of solar background at ground level as solar radiation is absorbed by ozone in the upper atmosphere. This can enable deployment of wide field-of-view receivers for better signal detection and low background noise for non-line-of-sight and line-of-sight communication.[48,50,51] Finally, we note that the two polymorphs, $D_{3h}$ and $D_{3d}$, exhibit similar electronic band structures and densities of states.[42] Thus, both polymorphs are important for UV-C sensing. In particular, their different symmetry (cen-

trosymmetry and axial symmetry in $D_{3d}$ and $D_{3h}$, respectively) could be critical for nonlinear optics, such as second harmonic generation, and for light polarization-dependent sensors.

## 3. Conclusion

In conclusion, we have demonstrated wafer-scale 2D semiconductors based on GaSe. The use of clean and controlled containment systems for handling the layers has made possible the development of a new centrosymmetric polymorph of GaSe, which is stabilized by in-plane tensile strain with the sapphire substrate. The layers are stable in air and exhibit uniform crystal symmetry and layer stacking properties over 2-in. wafers. We have used shadow masking to fabricate UV sensors based on nm-thick GaSe layers. The prototype concepts demonstrated in this work offer prospects for further developments of materials and designs toward scalable sensor arrays with enhanced sensitivity and imaging capability.

## 4. Experimental Section

*MBE Growth*: The MBE system (PRO-75) is capable of growth on rotating substrates with diameters of up to 3 in. The double-side polished $c$-plane (0001) sapphire substrates were initially annealed at 800 °C for 40 min to remove surface contamination. The substrate temperature was then reduced to 550 °C for the growth of GaSe. High-purity elemental Ga (7N) and Se (6N+) were evaporated from PEZ 63 production effusion and VSCS valved selenium cracker cells, respectively, both from Dr. Eberl MBE-Komponenten. The Ga beam flux was controlled by the temperature of the cell, while the Se flux was controlled by both the opening of the cracker valve and cell temperature. The growth was monitored by RHEED. The optimal growth conditions were achieved by exploring different Ga/Se flux ratios at a Ga cell temperature of 825 °C, and Se reservoir and cracker temperatures of 270 and 900 °C, respectively (Figure S9, Supporting Information). The GaSe growth rate under these conditions was estimated to be $\approx 1.7$ nm min$^{-1}$.

*Microscopy Studies*: The GaSe layer surface morphology was studied in situ by ncAFM, and ex situ using tapping and contact modes. In situ ncAFM was performed using a VT-AFM/XA microscope from Scienta Omicron. This technique involved frequency modulation where the cantilever was oscillated at a constant amplitude, and the frequency shift caused by tip-surface interactions was detected by a phase-locked loop. Ex situ AFM measurements were acquired using an Asylum Research Cypher-S AFM

ADVANCED
SCIENCE NEWS

www.advancedsciencenews.com

NANO · MICRO

small

www.small-journal.com

system under ambient conditions. Large scale topographic images were obtained in tapping mode using amplitude modulation, while lattice resolution images were acquired in contact mode using the lateral deflection channel. The high-resolution AFM analysis was conducted on multiple images from different regions of the sample, as well as across samples with different layer thicknesses. To reduce the effects of thermal drift and piezo creep, AFM images were acquired with a scan rate of 39 Hz, and lattice constant measurements were taken along all three lattice directions from scans in forward, backward, up, and down scanning directions. The data was processed using the Gwyddion software package.[52]

High-resolution high angle annular dark field (HR-HAADF) imaging in the STEM mode (camera length of 115 mm and probe convergence semiangle of 21.5 mrad) was used. EELS experiments were performed in the spectrum-imaging mode with an ultra high resolution energy filter (Gatan Quantum ERS), which allowed working in Dual-EELS mode (Core Loss/Low Loss). All microscopy studies were performed at 200 kV using a double aberration corrected Titan Cubed3 Themis FEI STEM microscope. It allowed the sample to be scanned under HRSTEM conditions with a probe size of 0.2 nm and a spatial resolution between 0.07 and 0.09 nm. EELS spectra were recorded at 29.5 mm of camera length and 41 mrad of collection angle.

X-ray photoelectron spectroscopy (XPS) was acquired using a SPECS DeviSim near ambient pressure XPS (NAP-XPS) instrument operating in ultra-high vacuum (UHV) mode at a pressure less than $1 \times 10^{-9}$ mbar. Spectra were measured using a Phoibos 150 NAP hemispherical analyzer with 20 eV pass energy and monochromatic Al K$\alpha$ X-rays (1486.7 eV). The samples were transported between the EPI2SEM system and XPS using a vacuum suitcase at a pressure less than $1 \times 10^{-10}$ mbar.

*Optical Studies*: Raman spectroscopy studies were performed in ambient conditions using a micro-Raman setup comprising a He–Ne laser (632.8 nm), an *x-y-z* motorized stage, and an optical confocal microscope system from Horiba Scientific (0.5 m-long monochromator and 1200 g mm$^{-1}$ grating). The signal was detected by a Si charge-coupled device camera. The laser beam diameter was focused to $\approx 1\ \mu$m using a 100× objective. Low excitation laser powers (up to 0.1 mW) were used to minimize heating.

The VASE measurements were performed on a M2000-DI (196 nm – 1700 nm) rotating compensator ellipsometer with focus probes (minor axis diameter 200 microns), from J.A. Woollam Co. at 55°, 60°, and 65° angles of incidence. Transmitted intensity measurements were also conducted at normal incidence close to the center of the wafer and these were incorporated into the initial modeling. The dielectric functions fitted to the measurements were modeled using CompleteEase v6.70. Further details of the modeling can be found in the Supporting Information.

*Density Functional Theory*: First-principles calculations were carried out within the framework of DFT by using the plane-wave pseudopotential approach as implemented in the VASP code. The generalized gradient approximation formulated by Perdew, Burke, and Ernzerhof was used as the exchange-correlation functional. Projected augmented wave pseudopotentials with the $3d^{10}4s^24p^1$ (Ga), $4s^24p^4$ (Se) treated explicitly as valence electrons were used. The kinetic energy cutoff for the plane wave basis was set to be 450 eV. To simulate single layer GaSe, vertical vacuum spaces with a thickness of 15 Å or more were adopted to separate the layers from their periodic images. The interlayer distance was optimized through total energy minimization including the vdW interaction using the optB86b- vdW functional, with the residual forces on the atoms, converged to below 0.01 eV Å$^{-1}$. A *k*-point grid spacing of $2\pi \times 0.03$ Å$^{-1}$ was adopted for electronic Brillouin zone integration in structure optimization calculation. For the optical calculations, the density of *k*-points in the mesh was increased to a spacing of $2\pi \times 0.015$ Å$^{-1}$. To remedy the band gap underestimation issue of DFT, a scissor operator with a magnitude equal to the band gap energy difference between the value calculated by DFT and that one from the measured absorption in bulk layers was used.

*Device Fabrication and Electrical Transport*: Electrical measurements were acquired using a Keithley 2400 Sourcemeter, a Keithley 2100 Multimeter, and an IV-converter. A continuous light spectrum from the VIS to the UV was provided by an Xe lamp. The output wavelength was selected using a HORIBA Jobin Yvon MicroHR monochromator. The power density

was estimated using a Thorlabs PM100D power meter. For the temporal response of the photocurrent, a mechanical chopper was used to modulate the incoming light. A Tektronix DPO 4032 oscilloscope with a 1 M$\Omega$ resistor and a 13 pF capacitor in series with the device was used for the measurement of the photocurrent. This combination of impedance and capacitance enables measurements of the frequency response at frequencies of up to $\approx$10 kHz. All transport measurements were conducted in a vacuum (pressure of $\approx 10^{-6}$ mbar).

## Supporting Information

Supporting Information is available from the Wiley Online Library or from the author.

## Conflict of Interest

The authors declare no conflict of interest.

## Data Availability Statement

The data that support the findings of this study are available from the corresponding author upon reasonable request.

[1] K. Khan, A. K. Tareen, M. Aslam, R. Wang, Y. Zhang, A. Mahmood, Z. Ouyang, H. Zhang, Z. Guo, *J. Mater. Chem. C* **2020**, *8*, 387.

[2] K. S. Novoselov, A. Mishchenko, A. Carvalho, A. Castro Neto, *Science* **2016**, *353*, 9439.

[3] X. Huang, C. Liu, P. Zhou, *npj 2D Mater. Appl.* **2022**, *6*, 51.

[4] P. V. Pham, S. C. Bodepudi, K. Shehzad, Y. Liu, Y. Xu, B. Yu, X. Duan, *Chem. Rev.* **2022**, *122*, 6514.

[5] S. K. Park, J. H. Kim, S. Y. Park, *Adv. Mater.* **2018**, *30*, 1704759.

[6] W. Deng, Y. Xiao, B. Lu, L. Zhang, Y. Xia, C. Zhu, X. Zhang, J. Guo, X. Zhang, J. Jie, *Adv. Mater.* **2021**, *33*, 2005915.

[7] X. Fang, J. Shi, X. Zhang, X. Ren, B. Lu, W. Deng, J. Jie, X. Zhang, *Adv. Funct. Mater.* **2021**, *31*, 2100237.

[8] A. K. Geim, I. V. Grigorieva, *Nature* **2013**, *499*, 419.

[9] X. Duan, C. Wang, J. C. Shaw, R. Cheng, Y. Chen, H. Li, X. Wu, Y. Tang, Q. Zhang, A. Pan, J. Jiang, R. Yu, Y. Huang, X. Duan, *Nat. Nanotechnol.* **2014**, *9*, 1024.

ADVANCED
SCIENCE NEWS

www.advancedsciencenews.com

NANO · MICRO
small
www.small-journal.com

[10] W. Liao, Y. Huang, H. Wang, H. Zhang, *Appl. Mater. Today* **2019**, *16*, 435.

[11] S. Wang, X. Liu, P. Zhou, *Adv. Mater.* **2022**, *34*, 2106886.

[12] S. Kang, D. Lee, J. Kim, A. Capasso, H. S. Kang, J.-W. Park, C.-H. Lee, G.-H. Lee, *2D Mater.* **2020**, *7*, 022003.

[13] S. Xie, M. Shiffa, M. Shiffa, Z. R. Kudrynskyi, O. Makarovskiy, Z. D. Kovalyuk, W. Zhu, K. Wang, A. Patanè, *npj 2D Mater. Appl.* **2022**, *6*, 61.

[14] Z. Yang, J. Hao, *Adv. Mater. Technol.* **2019**, *4*, 1900108.

[15] D. J. Terry, V. Zólyomi, M. Hamer, A. V. Tyurnina, D. G. Hopkinson, A. M. Rakowski, S. J. Magorrian, N. Clark, Y. M. Andreev, O. Kazakova, K. Novoselov, S. J. Haigh1, V. I. Fal'ko, R. Gorbachev, *2D Mater.* **2018**, *5*, 041009.

[16] D. Andres-Penares, A. Cros, J. P. Martinez-Pastor, J. F. Sanchez-Royo, *Nanotechnology* **2017**, *28*, 175701.

[17] J. F. Sánchez-Royo, G. Muñoz-Matutano, M. Brotons-Gisbert, J. P. Martínez-Pastor, A. Segura, A. Cantarero, R. Mata, J. Canet-Ferrer, G. Tobias, E. Canadell, J. Marqués-Hueso, B. D. Gerardot, *Nano Res.* **2014**, *7*, 1556.

[18] M. Song, N. An, Y. Zou, Y. Zhang, W. Huang, H. Hou, X. Chen, *Front. Phys.* **2023**, *18*, 52302.

[19] Q. Yu, F. Liu, Y. Zhang, H. Deng, B. Shu, J. Zhang, T. Yi, Y. Dai, C. Fan, W. Su, Z. Wang, S. Zhu, Z. Jiang, J. Wu, K. Zhang, *Adv. Photonics Res.* **2023**, *4*, 2200283.

[20] J. Jiang, L. Xu, C. Qiu, L.-M. Peng, *Nature* **2023**, *616*, 470.

[21] W. Han, X. Zheng, K. Yang, C. S. Tsang, F. Zheng, L. W. Wong, K. H. Lai, T. Yang, Q. Wei, M. Li, W. F. Io, F. Guo, Y. Cai, N. Wang, J. Hao, S. P. Lau, C.-S. Lee, T. H. Ly, M. Yang, J. Zhao, *Nat. Nanotechnol* **2023**, *18*, 55.

[22] H. Cai, Y. Gu, Y.-C. Lin, Y. Yu, D. B. Geohegan, K. Xiao, *Appl. Phys. Rev.* **2019**, *6*, 041312.

[23] D. V. Rybkovskiy, A. V. Osadchy, E. D. Obraztsova, *Phys. Rev. B.* **2014**, *90*, 235302.

[24] Z. B. Aziza, V. Zólyomi, H. Henck, D. Pierucci, M. G. Silly, J. Avila, S. J. Magorrian, J. Chaste, C. Chen, M. Yoon, K. Xiao, F. Sirotti, M. C. Asensio, E. Lhuillier, M. Eddrief, V. I. Fal'ko, A. Ouerghi, *Phys. Rev. B.* **2018**, *98*, 115405.

[25] M.-W. Chen, H. Kim, D. Ovchinnikov, A. Kuc, T. Heine, O. Renault, A. Kis, *NPJ 2D Mater. Appl.* **2018**, *2*, 2.

[26] G. Mudd, M. Molas, X. Chen, V. Zólyomi, K. Nogajewski, Z. R. Kudrynskyi, Z. D. Kovalyuk, G. Yusa, O. Makarovsky, L. Eaves, M. Potemski, V. I. Falko, A. Patanè, *Sci. Rep.* **2016**, *6*, 39619.

[27] D. A. Bandurin, A. V. Tyurnina, G. L. Yu, A. Mishchenko, V. Zólyomi, S. V. Morozov, R. K. Kumar, R. V. Gorbachev, Z. R. Kudrynskyi, S. Pezzini, Z. D. Kovalyuk, U. Zeitler, K. S. Novoselov, A. Patanè, L. Eaves, I. V. Grigorieva, V. I. Fal'ko, A. K. Geim, Y. Cao, *Nat. Nanotechnol.* **2017**, *12*, 223.

[28] E. A. Stepanov, V. Harkov, M. Rösner, A. I. Lichtenstein, M. I. Katsnelson, A. N. Rudenko, *npj Comput. Mater.* **2022**, *8*, 118.

[29] T. Cao, Z. Li, S. G. Louie, *Phys. Rev. Lett.* **2015**, *114*, 236602.

[30] K. Iordanidou, M. Houssa, J. Kioseoglou, V. Afanas' ev, A. Stesmans, C. Persson, *ACS Appl. Nano Mater.* **2018**, *1*, 6656.

[31] H. Bergeron, D. Lebedev, M. C. Hersam, *Chem. Rev.* **2021**, *121*, 2713.

[32] W. Mortelmans, S. De Gendt, M. Heyns, C. Merckling, *Appl. Mater. Today* **2021**, *22*, 100975.

[33] C. H. Lee, S. Krishnamoorthy, D. J. O'Hara, M. R. Brenner, J. M. Johnson, J. S. Jamison, R. C. Myers, R. K. Kawakami, J. Hwang, S. Rajan, *J. Appl. Phys.* **2017**, *121*, 094302.

[34] C.-W. Liu, J.-J. Dai, S.-K. Wu, N.-Q. Diep, S.-H. Huynh, T.-T. Mai, H.-C. Wen, C.-T. Yuan, W.-C. Chou, J.-L. Shen, H.-H. Luc, *Sci. Rep.* **2020**, *10*, 12972.

[35] E. Zallo, A. Pianetti, A. S. Prikhodko, S. Cecchi, Y. S. Zaytseva, A. Giuliani, M. Kremser, N. I. Borgardt, J. J. Finley, F. Arciprete, M. Palummo, O. Pulci, R. Calarco, *npj 2D Mater. Appl.* **2023**, *7*, 19.

[36] M. Yu, L. Murray, M. Doty, S. Law, *J. Vac. Sci. Technol. A* **2023**, *41*, 3.

[37] M. S. Claro, J. P. Martínez-Pastor, A. Molina-Sánchez, K. E. Hajraoui, J. Grzonka, H. P. Adl, D. Fuertes Marrón, P. J. Ferreira, O. Bondarchuk, S. Sadewasser, *Adv. Funct. Mater.* **2023**, *33*, 2211871.

[38] T. Yonezawa, T. Murakami, K. Higashimine, A. Fleurence, Y. Oshima, Y. Yamada-Takamura, *Surf. Interface Anal.* **2019**, *51*, 95.

[39] J. Grzonka, M. S. Claro, A. Molina-Sánchez, S. Sadewasser, P. J. Ferreira, *Adv. Funct. Mater.* **2021**, *31*, 2104965.

[40] W. Jie, X. Chen, D. Li, L. Xie, Y. Y. Hui, S. P. Lau, X. Cui, J. Hao, *Angew. Chem., Int. Ed.* **2015**, *54*, 1185.

[41] M. Al-Hattab, L. Moudou, Y. Chrafih, M. Khenfouch, O. Bajjou, K. Rahmani, *EPJ Appl. Phys.* **2020**, *91*, 30102.

[42] H. Nitta, T. Yonezawa, A. Fleurence, Y. Yamada-Takamura, T. Ozaki, *Phys. Rev. B.* **2020**, *102*, 235407.

[43] A. Kuhn, A. Chevy, R. Chevalier, *Phys. Status Solidi A* **1975**, *31*, 469.

[44] R. Hoff, J. Irwin, *Phys. Rev. B.* **1974**, *10*, 3464.

[45] M. R. Molas, A. V. Tyurnina, V. Zólyomi, A. K. Ott, D. J. Terry, M. J. Hamer, C. Yelgel, A. Babiński, A. G. Nasibulin, A. C. Ferrari, V. I. Fal'ko, R. Gorbachev, *Faraday Discuss.* **2021**, *227*, 163.

[46] H. Fujiwara, *Spectroscopic Ellipsometry: Principles and Applications*, John Wiley & Sons, Hoboken, NJ **2007**.

[47] D. Aspnes, *JOSA* **1980**, *70*, 1275.

[48] C. Xie, X.-T. Lu, X.-W. Tong, Z.-X. Zhang, F.-X. Liang, L. Liang, L.-B. Luo, Y.-C. Wu, *Adv. Funct. Mater.* **2019**, *29*, 1806006.

[49] S. Sorifi, P. Aggarwal, S. Kaushik, R. Singh, *ACS Appl. Electron. Mater.* **2023**, *5*, 451.

[50] N. Lim, J. Min, J.-H. Min, C. H. Kang, K.-H. Li, T.-Y. Park, W. Kim, B. Davaasuren, T. K. Ng, B. S. Ooi, D. H. Woo, J.-H. Park, Y. Pak, *Appl. Surf. Sci.* **2023**, *609*, 155350.

[51] L. Guo, Y. Guo, J. Wang, T. Wei, *J. Semicond.* **2021**, *42*, 081801.

[52] D. Nečas, P. Klapetek, *Cent. Eur. J. Phys.* **2012**, *10*, 181.